Research Square

Preprints are preliminary reports that have not undergone peer review.
They should not be considered conclusive, used to inform clinical practice,
or referenced by the media as validated information.

Three-Dimensional RANS Simulation of the Flow Field and Bed Shear Stress Around a Bridge Pier Combined with Abutments, with Collars and a Vertical Flow Deflector

Ahmed Shawky

bpc-1364@bpc.edu.sa

Benha University

Research Article

Keywords: CFD, OpenFOAM, bridge pier scour, collar, flow deflector, bed shear stress

Posted Date: November 26th, 2026

DOI: https://doi.org/10.21203/rs.3.rs-11541640/v1

License: This work is licensed under a Creative Commons Attribution 4.0 International License.
Read Full License

Additional Declarations: No competing interests reported.

Three-Dimensional RANS Simulation of the Flow Field and Bed Shear Stress Around a Bridge Pier Combined with Abutments, with Collars and a Vertical Flow Deflector

Abstract

Purpose: Local scour at a bridge pier that shares a contracted section with abutments is driven by a flow field that experiments alone cannot describe. This study uses numerical simulation to explain laboratory measurements of scour around a rectangular pier (3 cm × 20 cm) placed between two equal abutments in a 40 cm wide flume, without protection and with bed-level collars and a vertical plate flow deflector.

Methods: The steady Reynolds-averaged Navier–Stokes (RANS) equations were solved with the open-source code OpenFOAM (Open Source Field Operation and Manipulation), using the k–ω shear-stress transport (SST) turbulence model and Spalding's wall function. The model was validated against published velocity and bed-shear measurements in an equilibrium scour hole around a cylinder, and the numerical uncertainty was quantified with the grid convergence index (GCI) on three meshes. Flat-bed, scoured-bed and collar-in-hole cases were simulated at Froude numbers of 0.19–0.53.

Results: The model reproduced the peak downflow at the cylinder face ($-0.59U$ versus $-0.60U$ measured), its elevation and radial decay, and the onset of reversed bed shear. The approach-flow shear and the bed shear beyond about one pier width from the structures were mesh-independent (GCI < 5%), whereas the peak at the sharp pier corners was not. Bed shear was amplified about five times at the upstream corners, and the downflow at the pier nose increased from 0.41–0.43V on a flat bed to 0.82V in the equilibrium scour hole. Collars of width $B_c/b \geq 4$ reduced the peak shear on the exposed bed to about 2.5–2.8 times the approach value, and a collar inside the scour hole halved the downflow reaching the hole bottom and lowered the bottom shear from $0.93\tau_c$ to $0.41\tau_c$. The computed excess shear explained the measured relative

scour depth for 27 conditions (r = 0.95, R^2 = 0.89). A vertical plate deflector reduced the peak downflow by about 20%, and a plate height $d/b \approx 0.33$ gave the lowest shear ahead of the nose.

Conclusions: Collars and deflectors act mainly by intercepting the downflow at the pier nose; a collar of about 4b covers the strongly amplified region, and a deflector of height 0.33b agrees with the experimental optimum. Peak values at sharp corners are mesh-dependent and are interpreted qualitatively, and the results are limited to fixed beds and a rigid water surface.

Keywords: CFD; OpenFOAM; bridge pier scour; collar; flow deflector; bed shear stress

1. Introduction

Local scour at piers and abutments is driven by the downflow at the upstream face of the structure, the horseshoe vortex at its base, and the acceleration of flow around its sides (Dey 1995; Ettema et al. 2017; Melville and Coleman 2000; Wang et al. 2017). When a pier and abutments share a contracted section, these mechanisms interact with contraction effects (Melville 1997). Experiments give the final scour depth but little information about the flow that produces it. Computational fluid dynamics (CFD) has therefore been used increasingly to study the flow field and bed shear stress around piers, from early Reynolds-averaged Navier–Stokes (RANS) studies (Olsen and Melaaen 1993; Roulund et al. 2005; Salaheldin et al. 2004) to detached-eddy and large-eddy simulations (Khosronejad et al. 2012; Kirkil et al. 2008) and coupled flow–morphology models in OpenFOAM (Open Source Field Operation and Manipulation; Baykal et al. 2015; Chauchat et al. 2017). Similar methods have been applied to abutment-like obstructions (Koken and Constantinescu 2008) and to flow-altering countermeasures (Tafarojnoruz et al. 2010, 2012). For collars specifically, recent numerical studies used the commercial code FLOW-3D (Flow Science Inc., USA) and Eulerian–Lagrangian models with a mobile bed (Ebrahimi et al. 2024; Gupta et al. 2023, 2024), and collar systems were reviewed by Pasha et al. (2025). These studies concern isolated piers; none considered a pier sharing a contracted section with abutments.

Laboratory experiments were carried out on a pier–abutment system protected by collars of width 1.5–5*b* and by a vertical plate deflector combined with a 3*b* rectangular collar (Section 2.1). The present paper uses three-dimensional RANS simulations to (i) describe the flow and bed shear stress around the unprotected system at three Froude numbers; (ii) quantify how collars of different widths shield the high-shear zones; (iii) relate the computed bed shear, through the critical shear stress of the experimental sand, to the measured scour depths; (iv) examine the flow inside an equilibrium scour hole, with and without a collar; and (v) explain the effect of deflector height and width. Particular attention is paid to model credibility: the model is validated against published velocity and bed-shear measurements around a cylinder in a scour hole (Graf and Istiarto 2002; Istiarto 2001), and numerical uncertainty is quantified through a three-mesh grid-convergence study and a comparison of two wall treatments.

2. Materials and methods

2.1 Laboratory experiments

The experiments were carried out in a university hydraulics laboratory [details removed for anonymous review], in a recirculating flume 15 m long, 0.40 m wide and 0.60 m deep with a horizontal bed; the test section was located at the middle of the flume. The bed in the test section consisted of uniform sand with d_{50} = 0.5 mm and geometric standard deviation σ_g = 1.1. A rectangular pier (b = 3 cm wide, 20 cm long) was placed on the flume center line between two abutments of the same size (3 cm protrusion, 20 cm length) fixed to the side walls at the same cross-section (Fig. 1), reducing the flow width from 40 to 31 cm. All runs used a discharge Q = 3.5 l/s. The tailwater depth y was set to 3, 3.5, 4, 5 and 6 cm (and 4.5 and 5.5 cm in the deflector runs), giving approach velocities of 0.14 – 0.29 m/s and Froude numbers of 0.19–0.53. Each run lasted 6 h. The flume was then drained, and the maximum scour depth d_s, its location and the maximum deposition height were measured with a point gauge.

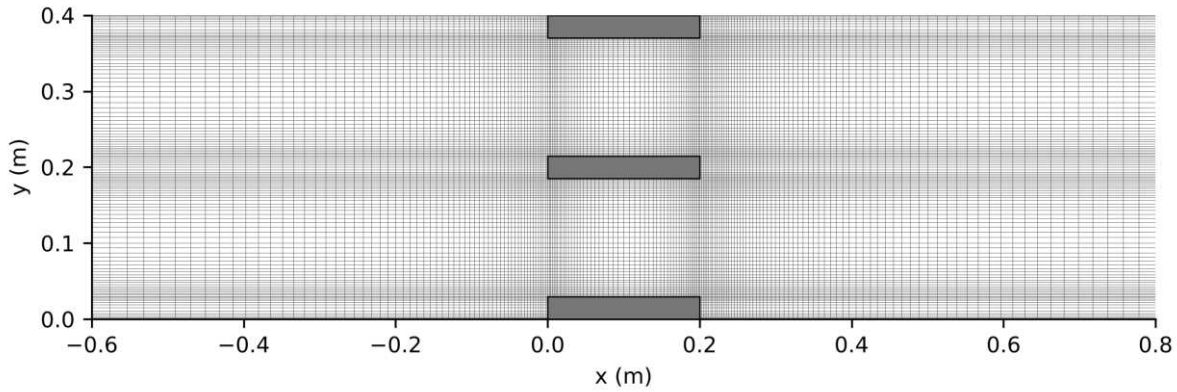


Fig. 1. Plan view of the medium computational mesh at the bed (pier and abutments in grey).

Five groups of runs were made: (1) no protection; (2) thin rectangular collars placed at the original bed level around the pier and both abutments, extending $(B_c - b)/2$ beyond each exposed face, with relative widths B_c/b = 1.5, 2, 2.5, 3, 3.5, 4, 4.5 and 5, tested in four series (A–D); (3) a vertical plate deflector attached to the pier nose, with height d measured from the bed (0.5–1.5 cm) and transverse width L = 4.5 cm, combined with a 3b rectangular collar; (4) the same deflector with width L = 3–12 cm; and (5) inclined deflectors and additional side deflectors. Groups 1–4 are used in this paper. Table 1 summarizes the measured scour depths used for comparison with the simulations; the collar values are the mean (and range) of configurations A–D. Without protection the relative scour depth d_s/y ranged from 0.22 at Fr = 0.19 to 1.22 at Fr = 0.53. The scour reduction increased with collar width, and collars of $B_c/b \geq$ 4.5 prevented scour at Fr ≤ 0.25 in all configurations. Adding a deflector with d = 1 cm (d/b = 0.33) to the 3b collar reduced the scour depth at Fr = 0.53 from 1.7–2.1 cm (collar alone) to 1.30 cm. The deflector heights d = 0.5, 0.75, 1.0, 1.25 and 1.5 cm gave 1.55, 1.43, 1.30, 1.40, 1.45 cm respectively, while the width L had little effect (1.35–1.60 cm).

Table 1. Measured maximum scour depth ds (cm) at the three depths simulated; collar values are the mean (range) of configurations A–D.

B_c/b	y = 3 cm (Fr = 0.53)	y = 4 cm (Fr = 0.35)	y = 6 cm (Fr = 0.19)
No collar	3.65	3.10	1.30
1.5	3.06 (2.95–3.25)	2.10 (1.50–2.60)	0.44 (0.30–0.60)
2.0	2.56 (2.45–2.80)	1.72 (1.20–2.20)	0.16 (0.10–0.20)
2.5	2.19 (2.10–2.25)	0.88 (0.70–1.05)	0.15 (0.10–0.20)

B_c/b	y = 3 cm (Fr = 0.53)	y = 4 cm (Fr = 0.35)	y = 6 cm (Fr = 0.19)
3.0	1.91 (1.70–2.10)	0.55 (0.50–0.60)	0.05 (0.00–0.10)
3.5	1.64 (1.40–1.80)	0.47 (0.40–0.55)	0.03 (0.00–0.10)
4.0	1.25 (1.05–1.55)	0.35 (0.30–0.40)	0.00
4.5	1.09 (0.90–1.25)	0.27 (0.20–0.35)	0.00
5.0	0.99 (0.80–1.20)	0.20 (0.15–0.25)	0.00

2.2 Numerical model

2.2.1 Governing equations and solver

The incompressible, steady RANS equations were solved with the SIMPLEC (Semi-Implicit Method for Pressure-Linked Equations–Consistent) algorithm (simpleFoam, OpenFOAM v1912; Weller et al. 1998). Turbulence was modelled with the k–ω shear-stress transport (SST) model (Menter 1994), which performs well in adverse-pressure-gradient flows such as the stagnation region upstream of a pier (Salaheldin et al. 2004). The convection term of momentum was discretised with a bounded second-order linear-upwind scheme and the turbulence equations with a limited-linear scheme. Near-wall turbulent viscosity was given by Spalding's (1961) continuous law of the wall, which is valid throughout the viscous sublayer, buffer layer and log layer. This choice matters here: with the standard wall function, which switches abruptly between laminar and logarithmic behaviour at $y^+ = 11.5$, the near-wall y^+ at the shear peaks (≈ 11–18) fell on different sides of the switch on different meshes (Section 2.2.5). The bed shear stress was computed as $\tau/\rho = (\nu + \nu_{t,w})|U_{t,P}|/y_P$, where $U_{t,P}$ is the wall-parallel velocity at the first cell center.

2.2.2 Domain, mesh and boundary conditions

The computational domain reproduces the flume section (Fig. 1): width B = 0.40 m, length 1.40 m (0.60 m upstream and 0.60 m downstream of the structures), with the pier (3 × 20 cm) on the center line and the two abutments (3 × 20 cm) on the side walls. A structured hexahedral mesh was generated with blockMesh, refined towards all solid surfaces and the bed. The medium (production) mesh had 305,280 cells with 16 cells over the depth and a mean bed $y^+ \approx 8$;

115 deflector cases required additional blocks (≈ 388,500 cells). Table 2 lists the boundary
116 conditions.

117 **Table 2.** Boundary conditions.

Boundary	Velocity	Pressure	k, ω, ν_t
Inlet	1/7 power-law profile, depth-average $V = Q/(By)$	zero gradient	fixed: I = 5 %, $\ell = 0.07y$
Outlet	inlet–outlet	fixed (0)	inlet–outlet
Bed, walls, structures	no-slip	zero gradient	wall functions (Spalding for ν_t)
Free surface	symmetry (rigid lid)	symmetry	symmetry

118
119 2.2.3 Simulated cases and convergence
120 Three flow depths were simulated with the laboratory discharge Q = 3.47 l/s: y = 3, 4 and 6 cm
121 (V = 0.289, 0.217 and 0.145 m/s; Fr = 0.53, 0.35 and 0.19). Four deflector cases were run at Fr
122 = 0.53: a vertical plate 3 mm thick attached to the pier nose, with height d measured from the
123 bed (d/b = 0.17, 0.33, 0.50) and transverse width $L = 1.5b$, plus d/b = 0.33 with $L = 3b$. One
124 further case used an idealized equilibrium scour hole (Section 2.2.6). Each case ran 1500
125 iterations. Residuals levelled off after about 200 iterations because of weak unsteadiness in the
126 wakes; continuing a preliminary run from 2000 to 2400 iterations changed the peak bed-shear
127 amplification by less than 0.5 %. All results are presented as amplification relative to each
128 mesh's own approach shear τ_0 (mean over 0.25 m ≤ $-x$ ≤ 0.35 m, 0.05 m ≤ y ≤ 0.35 m). The
129 computed approach shear velocities (17.0, 12.8 and 8.6 mm/s) agree within 8 % with the
130 smooth-wall logarithmic law (15.7, 11.8 and 7.9 mm/s).

131 2.2.4 Representation of collars
132 The collars in the experiments were thin plates at bed level. On a flat, fixed bed a flush collar
133 does not change the flow, because the bed and the collar are both no-slip surfaces. Its effect at
134 the start of scouring is to shield the bed beneath it. Collars were therefore represented by
135 removing their footprint, an extension of $(B_c - b)/2$ around each structure, from the erodible
136 bed, and the shear on the remaining exposed bed was evaluated to be within 0.15 m ≤ x ≤ 0.45
137 m. Two measures were used: the peak value $A_{max} = \max(\tau/\tau_0)$, and the area-averaged

amplification A_{band} over a strip of width b beyond the collar edge. This approach captures the shielding effect but not the later interaction between the collar and a developing scour hole, which requires a mobile-bed model (Ebrahimi et al. 2024; Gupta et al. 2024).

2.2.5 Mesh independence

Three systematically refined meshes were used for Fr = 0.53: coarse (101,640 cells), medium (305,280) and fine (825,132), with refinement ratios r_{21} = 1.39 and r_{32} = 1.44. The grid convergence index (GCI) was evaluated following Celik et al. (2008); Table 3 and Fig. 2 summarize the results. The approach shear, the peak shear outside 3b and 4b collars, and the band-averaged shear for $B_c/b \geq 2.5$ are mesh-independent within about 5 %. The downflow converges monotonically but more slowly (GCI ≈ 19 %). The peak shear without a collar, which occurs within a few millimeters of the sharp upstream corners of the pier and abutments, keeps increasing with refinement (GCI ≈ 42 %). This is expected at a sharp convex corner, where the RANS solution has no mesh-independent maximum. Results that depend on that peak (no collar and narrow collars, $B_c/b \leq 2$) are therefore interpreted qualitatively, and the conclusions rest on the converged quantities.

Table 3. Grid-convergence study (Fr = 0.53). GCI refers to the fine mesh.

Quantity	Coarse	Medium	Fine	Apparent order p	GCI (%)
u_{*0} (m/s)	0.017	0.017	0.017	–	3.7
$\|w\|_{max}/V$ at pier nose	0.370	0.414	0.442	1.05	18.8
A_{max}, no collar (corner)	3.994	4.923	6.254	1.48	42.2
A_{max} outside 3b collar	3.299	3.902	4.090	3.03	3.3
A_{max} outside 4b collar	2.543	2.749	2.844	1.91	4.7

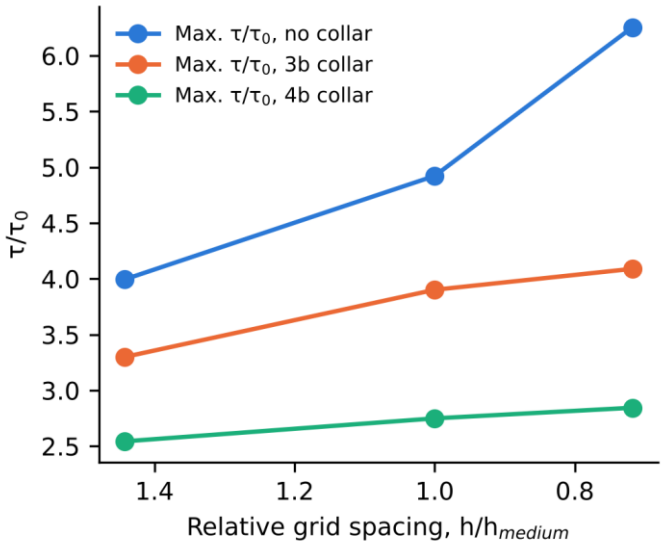


Fig. 2. Peak bed shear amplification on three meshes: the corner peak (no collar) is mesh-dependent, the values outside 3b and 4b collars converge.

The wall treatment was also tested. With the standard wall function the medium-mesh peak amplification without a collar was 3.54, compared with 4.92 with Spalding's law, but the trends with Fr and collar width were the same, and the correlation with the measured scour (Section 3.4) was $r = 0.91$ and 0.95, respectively. The conclusions are therefore not sensitive to the wall treatment.

2.2.6 Scoured-bed geometry

To examine the flow at the end of the scour process, the medium mesh was deformed to an idealized equilibrium hole around each structure. The hole had the measured maximum depth for the unprotected case at Fr = 0.53 (d_s = 3.65 cm) at the structure faces and side slopes at the angle of repose (32°), giving a hole radius of 5.8 cm; mesh lines were stretched vertically between the deformed bed and the free surface (maximum non-orthogonality 32°). The real hole is asymmetric and shallower downstream, so this case is used to study the flow mechanisms rather than to reproduce the measured bed.

To simulate a collar inside a scour hole, a second family of meshes (457,920 cells, 24 cells over the depth) was used, in which one mesh level is held flat at the original bed level over the hole, so that the collar can be inserted as a thin, zero-thickness wall (baffle) at $z = 0$. Three cases were

run at Fr = 0.53: the 3.65 cm hole without a collar, the same hole with a 3b collar around each structure, and a 3b collar with the equilibrium depth measured for that collar (mean of configurations A–D, d_s = 1.91 cm, hole beneath the collar and sloping beyond its edge).

2.2.7 Validation against published measurements

Because velocities were not measured in the present experiments, the model was validated against the detailed acoustic Doppler velocity profiler (ADVP) measurements of Istiarto (2001) and Graf and Istiarto (2002) around a cylinder (D = 0.15 m) in an equilibrium scour hole in a 2.45 m wide flume (h = 0.18 m, U_∞ = 0.45 m/s, Fr = 0.34, d_{50} = 2.1 mm, d_s = 25 cm at the leading edge). The same solver, schemes and turbulence model were used. Half of the channel was modelled with a symmetry plane, an O-grid around the cylinder (128k and 355k cells), the measured hole geometry (depth 25, 24, 21.3 and 19 cm and outer radius 45, 52, 90 and 105 cm at 0°, 90°, 135° and 180°), a rough-wall function on the sand bed ($k_s = d_{50}$) and a logarithmic inflow profile. Table 4 and Fig. 3 compare the results. The computed approach shear (0.77 Pa) is close to the measured 0.70 Pa. At the cylinder face (r = 10 cm) the peak downflow is $-0.59U_\infty$ at 0.44 of the local depth above the bed, against $-0.60U_\infty$ at 0.40 measured; at the original bed level it is $-0.48U_\infty$ (−0.40 measured). The radial decay of the maximum downflow follows the empirical decay relation proposed by Istiarto (2001) within a root-mean-square (RMS) difference of 0.04. Reversed (upstream-directed) bed shear begins at x = −42 cm, where the measurements show the sign change between −42 and −44 cm. The depth-averaged velocity along the upstream plane is reproduced with r = 0.96 and a mean absolute error of $0.08U_\infty$. The model underestimates it by about $0.1–0.15U_\infty$ on the hole slope (20 cm ≤ r ≤ 40 cm). The jump in the measured values at r < 20 cm reflects the partial profiles there, which cover only the lowest 5 cm of the water column. The reversed shear near the cylinder is over-predicted (about −0.5 Pa against −0.1 to −0.3 Pa), in the corner region where the rough-wall function and the velocity-based shear estimate are both least reliable. The two meshes give nearly identical

results. Overall, the model reproduces the downflow and the horseshoe-vortex footprint, the quantities on which this study relies.

Table 4. Validation against the measurements of Istiarto (2001) and Graf and Istiarto (2002).

Quantity	Measured	CFD 128k	CFD 355k
Approach bed shear τ_0 (Pa)	0.70	0.78	0.77
Peak downflow at r = 10 cm, w/U_∞	−0.60	−0.57	−0.59
Elevation of peak, $(z - z_b)/(h - z_b)$	0.40	0.46	0.44
Downflow at original bed level, w/U_∞	−0.40	−0.48	−0.48
Start of reversed bed shear, x (cm)	−42 to −44	−41	−42
Depth-averaged u/U_∞: r / MAE	–	0.96 / 0.09	0.96 / 0.08
Radial decay of w_{max}: RMS difference	–	0.04	0.04

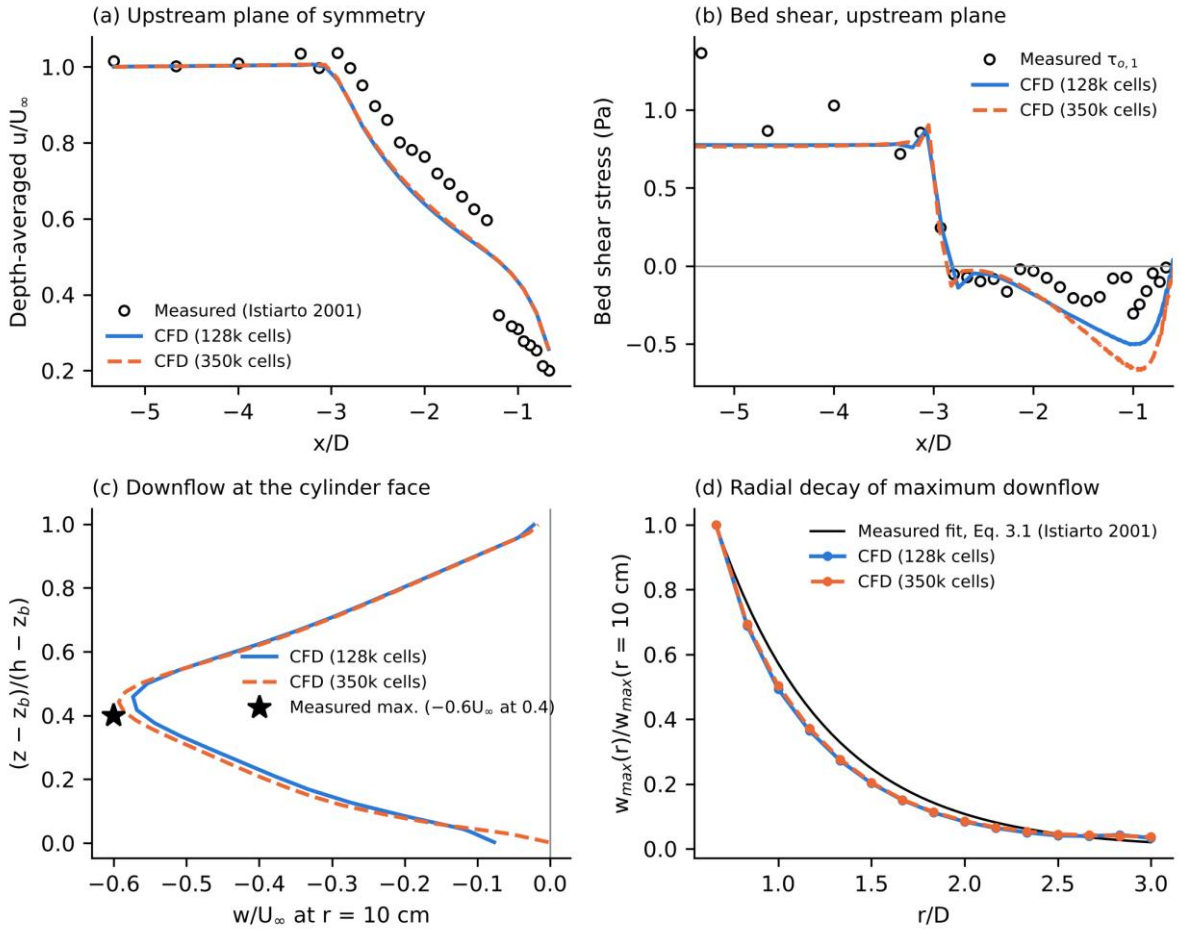


Fig. 3. Validation against Istiarto (2001): (a) depth-averaged velocity and (b) bed shear along the upstream plane of symmetry; (c) downflow profile at r = 10 cm; (d) radial decay of the maximum downflow.

3. Results and discussion

3.1 Flow field around the pier–abutment system

Fig. 4 shows the velocity magnitude and streamlines at mid-depth and near the bed for Fr = 0.53. The structures contract the flow section from 40 to 31 cm, and the flow accelerates through the two openings to about 1.3–1.6V. The highest velocities occur along the upstream half of the pier sides and the inner faces of the abutments. Separation at the upstream corners creates recirculation zones along the sides and in the wakes. Near the bed, the streamlines diverge ahead of the pier nose and converge towards the sides, which shows near-bed fluid being swept sideways to feed the horseshoe vortex.

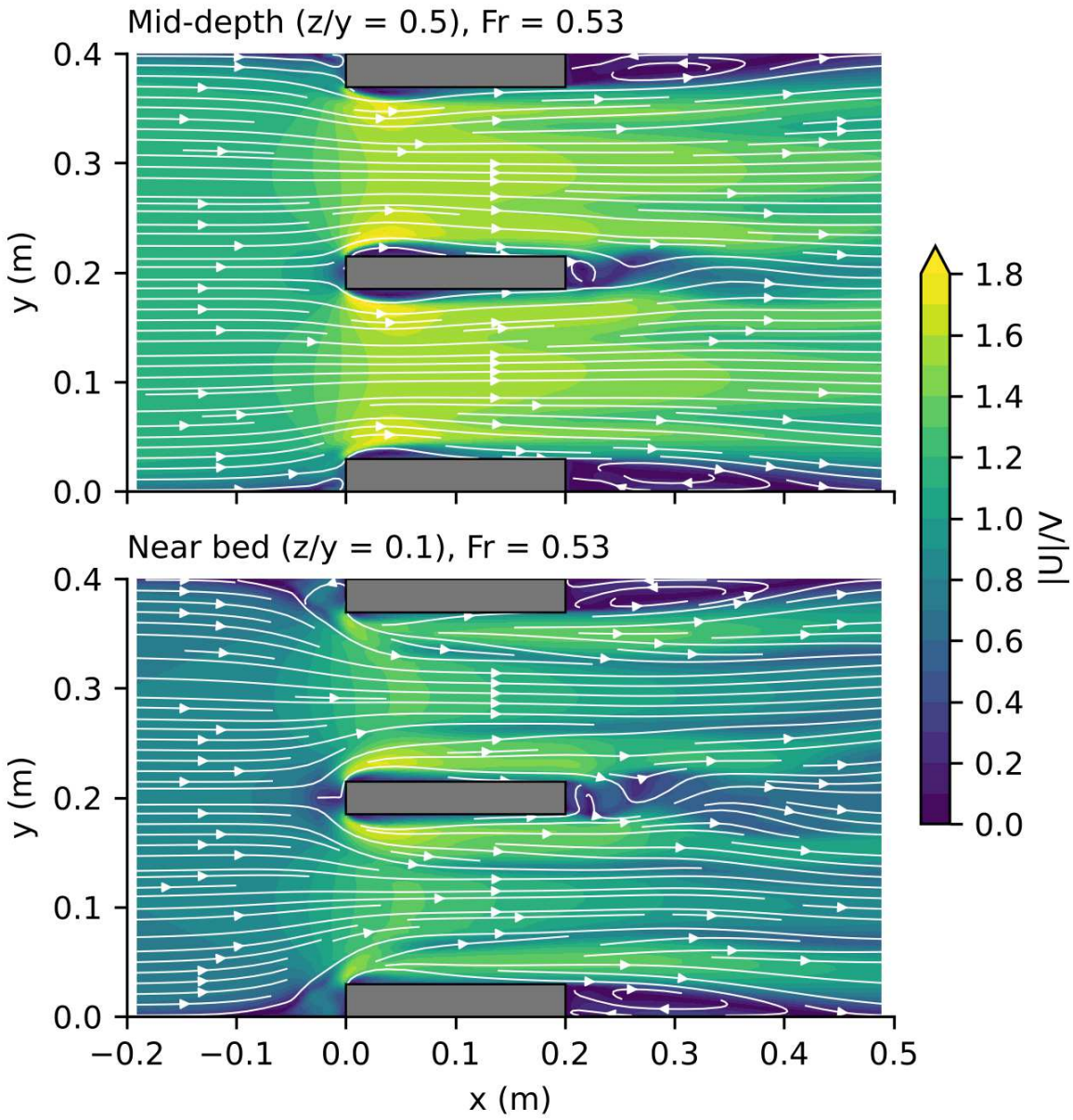


Fig. 4. Velocity magnitude and streamlines at mid-depth and near the bed (Fr = 0.53).

The vertical center plane upstream of the pier (Fig. 5) shows the stagnation pressure turning the approach flow downward over about one pier width upstream of the nose. The downflow profile at the nose (Fig. 6) reaches a maximum of 0.41–0.43V at $z/y \approx 0.18$–0.26, within the 0.4–0.5V range reported for cylindrical piers (Melville and Coleman 2000; Raudkivi 1986). On a flat bed the horseshoe vortex is weak and confined to the corner. It strengthens once a scour hole forms (Section 3.5), a known limitation of flat-bed simulations (Baykal et al. 2015; Roulund et al. 2005).

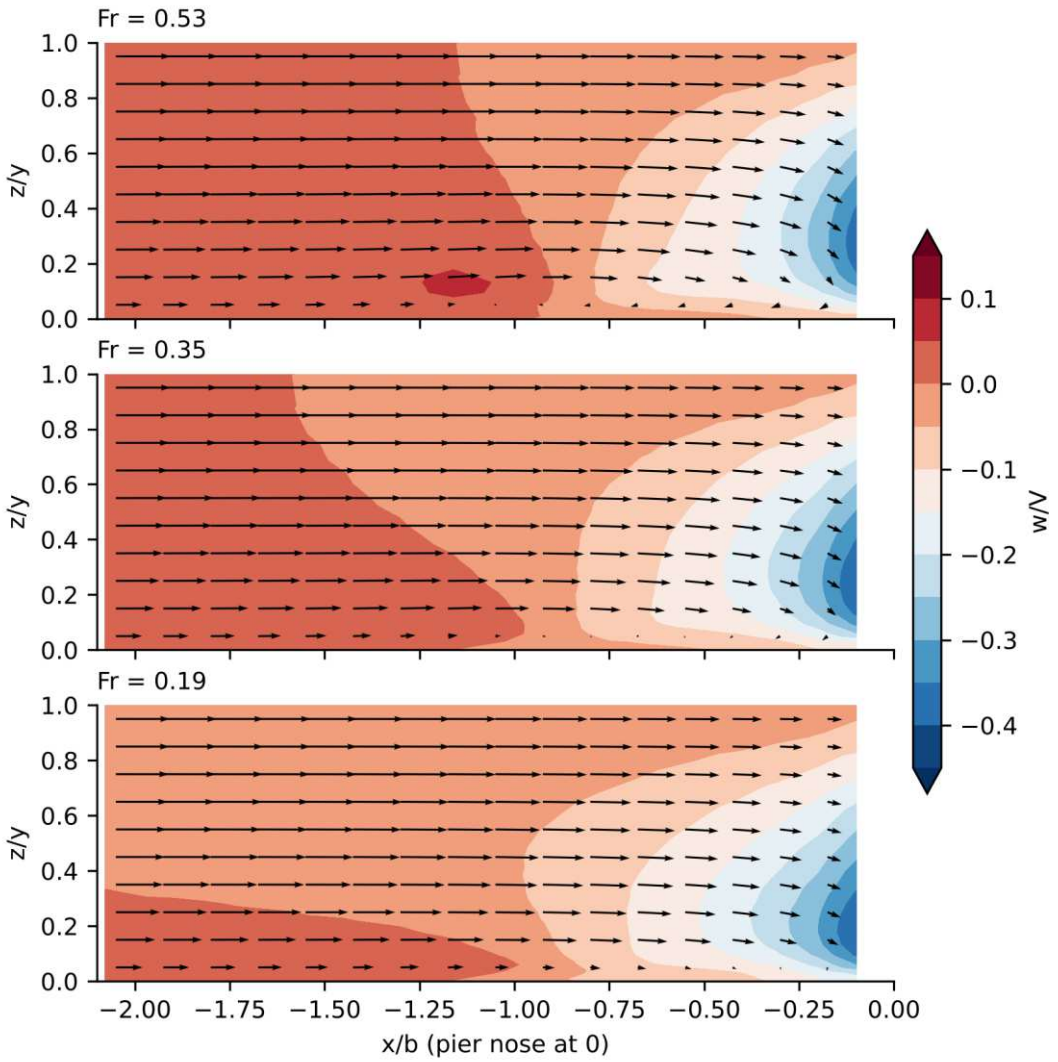


Fig. 5. Vertical velocity (colour) and velocity vectors in the centre plane upstream of the pier nose (flat bed).

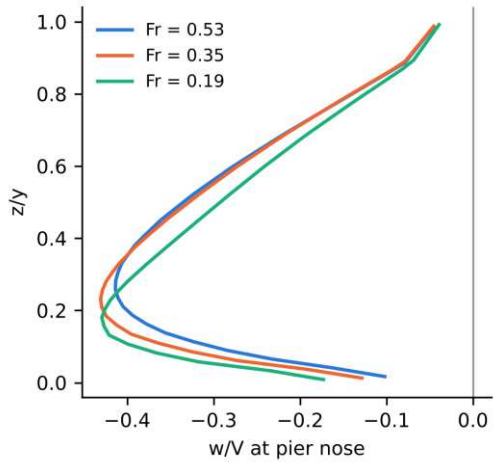


Fig. 6. Downflow profiles at the pier nose (flat bed).

3.2 Bed shear stress

Fig. 7 maps the bed shear amplification τ/τ_0. The highest values occur at the upstream corners of the pier and abutments and along the first quarter of their sides. On the medium mesh they are about 4.9 at the pier and 3.83–4.91 at the abutments; as shown in Section 2.2.5, these corner values are mesh-dependent. A low-shear zone lies just upstream of the pier nose, at the stagnation point, and long low-shear wakes extend downstream. This pattern matches the experiments: the deepest scour was found just upstream and beside the structures, and the eroded sediment was deposited downstream. The amplification at the pier is almost independent of Fr, whereas at the abutments it decreases as the depth increases, which shows that the flow structure at the abutments changes with depth.

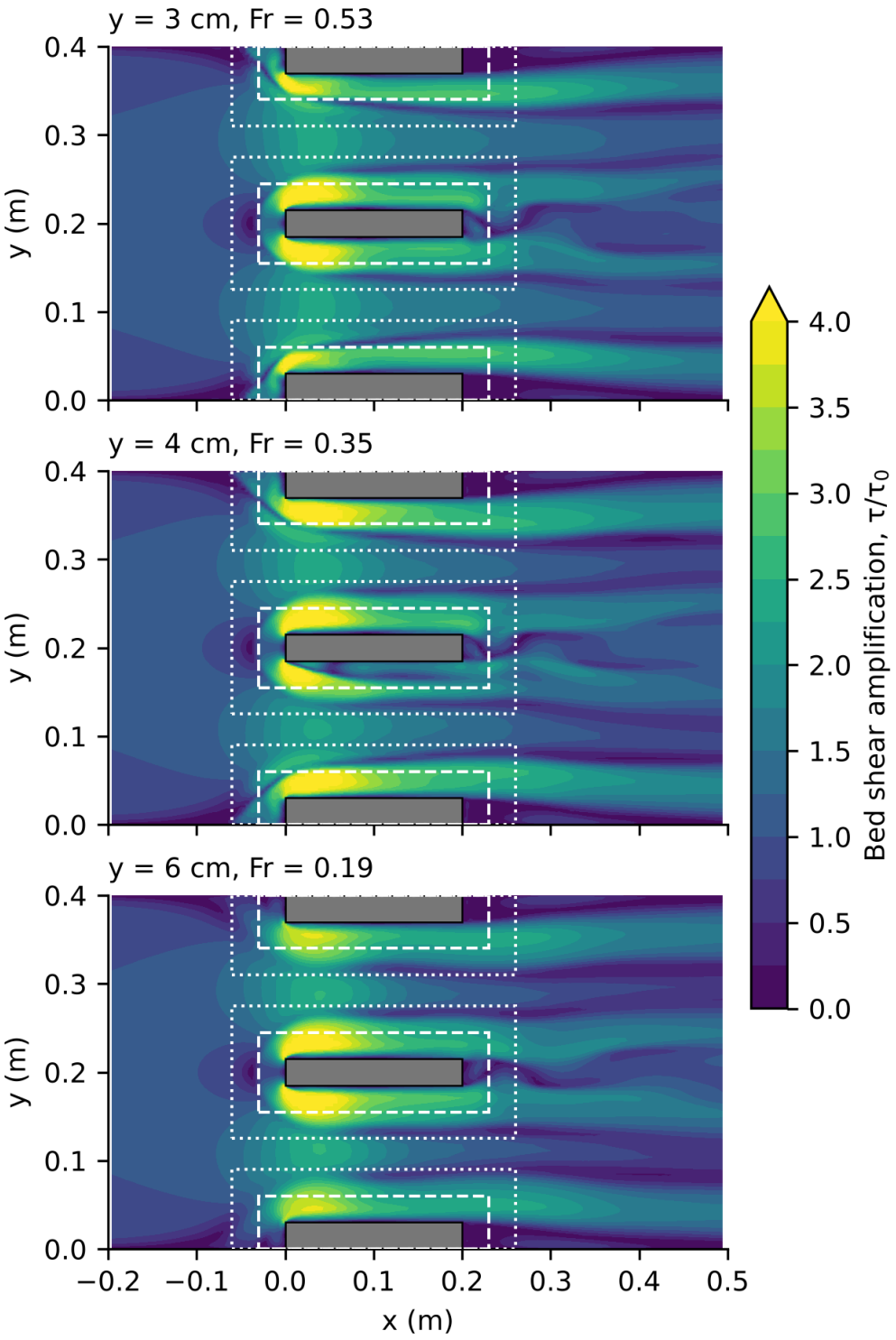


Fig. 7. Bed shear amplification τ/τ0 at three Froude numbers; dashed and dotted lines show the footprints of 3b and 5b collars.

3.3 Shielding by collars

Fig. 8 shows the peak amplification on the exposed bed versus collar width. Narrow collars ($B_c/b \leq 2$) leave the peak almost unchanged, because the high-shear zone at the corners extends beyond their edge. The peak falls rapidly between B_c/b = 2.5 and 4 and then stays nearly

constant at 2.51–2.75, values that are mesh-independent (Table 3). The band-averaged amplification follows the same trend (from 2.02 at 2b to 1.52 at 4b for Fr = 0.53). A collar of about 4b therefore covers the strongly amplified region, and wider collars give little additional benefit. The experiments showed the same diminishing return beyond $B_c/b \approx 4$.

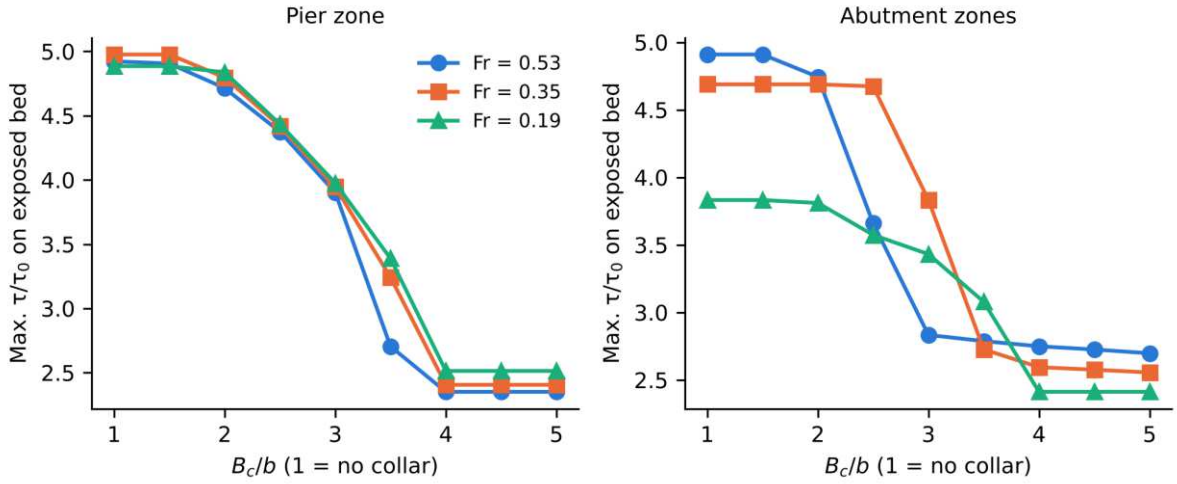


Fig. 8. Peak bed shear amplification on the exposed bed versus collar width.

3.4 Comparison with the experiments

The critical shear velocity of the experimental sand (d_{50} = 0.5 mm, s = 2.65) is u_{*c} = 15.8 mm/s from the Shields curve in the form of Soulsby (1997), i.e. $\tau_c/\rho = 2.50 \times 10^{-4}$ m²/s². The approach flow was therefore close to the threshold of motion at Fr = 0.53 (u_{*0}/u_{*c} = 1.08) and clearly below it at Fr = 0.35 and 0.19 (0.81 and 0.54). The amplification alone is almost independent of Fr, so it cannot explain why the same collar is much more effective at low Fr (Fig. 9, left). A combined indicator was therefore defined as the excess shear $\tau_{max}/\tau_c - 1$, where $\tau_{max} = A_{max}\tau_0$ is the computed peak shear on the exposed bed. The measured relative scour depth increases linearly with this indicator (Fig. 9, right), as expressed by Eq. (1):

$$\frac{d_s}{y} = 0.205\left(\frac{\tau_{max}}{\tau_c} - 1\right) \qquad (1)$$

with r = 0.95 and R^2 = 0.89 over 27 conditions (3 Froude numbers × 9 collar widths). Because τ_c comes from the measured grain size, the relation involves no fitted threshold. Restricting the comparison to the mesh-independent conditions ($B_c/b \geq 2.5$, 18 conditions) gives r = 0.95 with

the peak shear and $r = 0.93$ with the band-averaged shear, so the agreement does not depend on the uncovered corner values.

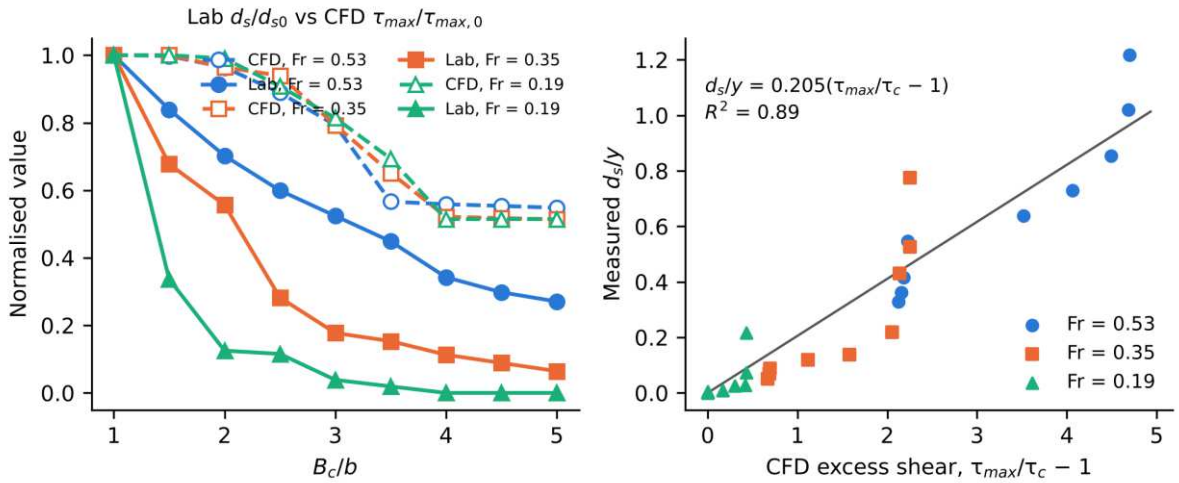


Fig. 9. Comparison with the experiments: (left) normalised scour and computed peak shear versus collar width; (right) measured ds/y versus computed excess shear, with τc from the Shields criterion for d50 = 0.5 mm.

3.5 Flow inside the equilibrium scour hole

Fig. 10 compares the centre-plane flow over the flat and scoured beds. Inside the hole the downflow penetrates to the bottom and doubles in strength, reaching $0.82V$ at $z/y \approx -0.35$, i.e. below the original bed level. Along the upstream slope a strong horseshoe vortex forms: the near-bed velocity is reversed (towards the pier) with magnitude up to $0.66V$, over a distance of $1.6b$ upstream of the nose. This confirms that the downflow captured at the start of scour is the driver that later sustains the vortex. A countermeasure that weakens it, such as a collar or deflector, therefore acts on the main scour mechanism. The mean bed shear at the bottom of the hole is 0.93–1.24 times the critical value, depending on the mesh family (0.98 with the standard wall function), i.e. close to the threshold expected at equilibrium. This gives an independent check of the model, the measured scour depth and the Shields-based τ_c.

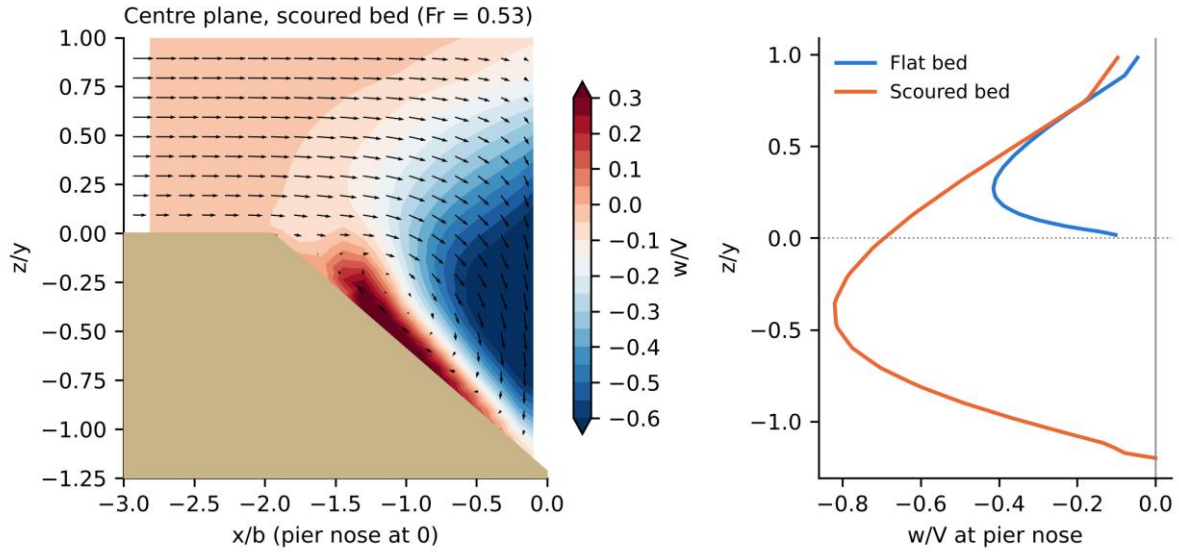


Fig. 10. Flow at the pier nose over the idealised equilibrium scour hole (Fr = 0.53): (left) vertical velocity and vectors in the centre plane; (right) downflow profiles over the flat and scoured beds.

3.6 Collar inside the scour hole

Fig. 11 shows how a 3*b* collar changes the flow in the same 3.65 cm hole. Without a collar, the downflow runs down the pier face to the bottom of the hole ($-0.82V$). With the collar, the downflow is intercepted at bed level: below the collar at the pier nose, it falls to $-0.41V$, and the main downward jet is displaced to the collar edge ($x \approx -b$), where it is weaker ($-0.70V$). Beneath the collar a recirculation with upward velocity develops. The mean shear at the hole bottom drops from $0.93\tau_c$ to $0.41\tau_c$, and the fraction of the hole surface near the pier where $\tau > \tau_c$ from 73 % to 46 %. A hole of this depth could therefore not be sustained with the collar in place, which explains why the collar limits the equilibrium depth. For the 3*b* collar with its own measured equilibrium hole (d_s = 1.91 cm), the downflow under the collar is almost eliminated ($-0.11V$) and the bottom shear is $0.73\tau_c$, below but close to the threshold. The equilibrium holes measured with and without the collar thus both end with the bottom shear near critical (0.7–1.2τ_c). This consistency supports both the measurements and the model, and it shows that the collar works by blocking the downflow rather than only by covering the bed.

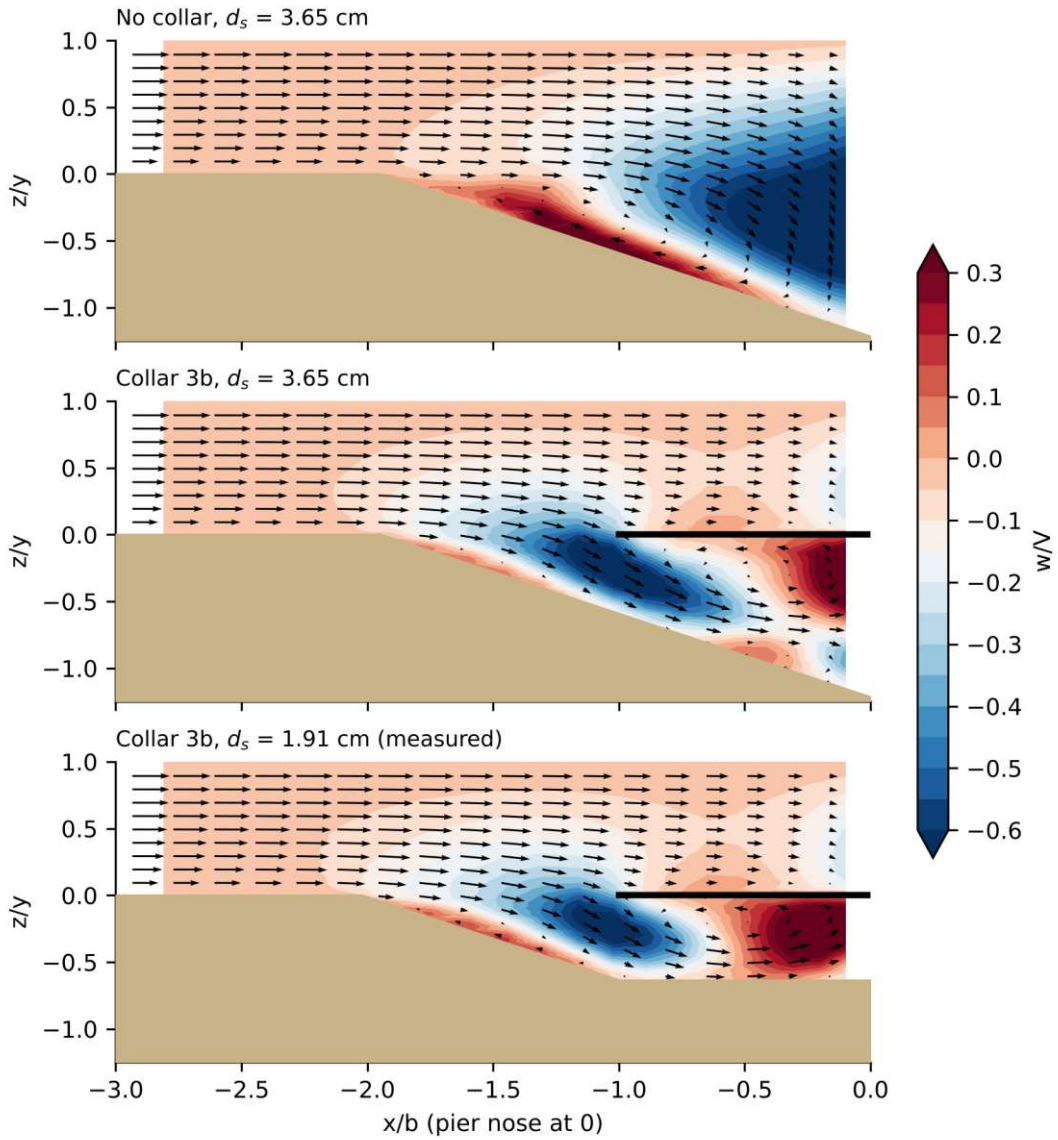


Fig. 11. Vertical velocity and vectors in the centre plane with the collar modelled as a thin plate (black line) at bed level: (top) no collar, 3.65 cm hole; (middle) 3b collar, same hole; (bottom) 3b collar with its measured equilibrium hole (1.91 cm).

3.7 Vertical plate deflector

Table 5 and Figs. 12–13 summarize the deflector simulations. All plates reduced the peak downflow ahead of the nose from 0.41V to 0.32–0.34V (−17 to −22 %). The plate stops the lower part of the downflow and turns it upstream and sideways, producing a small vortex ahead of the plate (Fig. 12). Sections 3.5–3.6 showed that the downflow drives the horseshoe vortex in the scour hole, so this reduction is the main mechanism by which the deflector improved the performance of the 3*b* collar in the experiments (reduction from 43–53 % to about 64 % at Fr = 0.53).

The plate height controls where the deflected flow reaches the bed. With $L = 1.5b$, the nose-zone amplification was 4.96 for $d/b = 0.17$, 4.33 for 0.33 and 4.57 for 0.50, compared with 3.30 without a plate. The intermediate height therefore gives the most favorable compromise, in agreement with the optimum $d/b \approx 0.25$–0.33 found in the experiments. Widening the plate to $3b$ lowered the nose-zone shear (2.72) but concentrated shear at the plate edges (peak 5.48 without a collar), which explains why longer deflectors brought no additional benefit in the laboratory. On a flat bed none of the plates reduced the peak shear at the collar edge beside the pier, which is controlled by the flow acceleration around the sides. The nose-zone values lie close to the plate and pier corners, so they should be read as relative comparisons between plates on the same mesh rather than as mesh-independent magnitudes.

Table 5. Deflector simulations at Fr = 0.53 (Spalding wall function; amplification relative to each mesh's approach shear).

Case	Peak downflow /V	Near-bed /V	A nose zone	A_{max} pier, no collar	A_{max} pier, $3b$ collar
No deflector	0.41	0.23	3.30	4.92	3.90
d/b=0.17, L/b=1.5	0.32	0.19	4.96	5.00	4.07
d/b=0.33, L/b=1.5	0.33	0.19	4.33	4.39	3.90
d/b=0.50, L/b=1.5	0.34	0.19	4.57	4.79	4.42
d/b=0.33, L/b=3	0.33	0.18	2.72	4.79	4.79

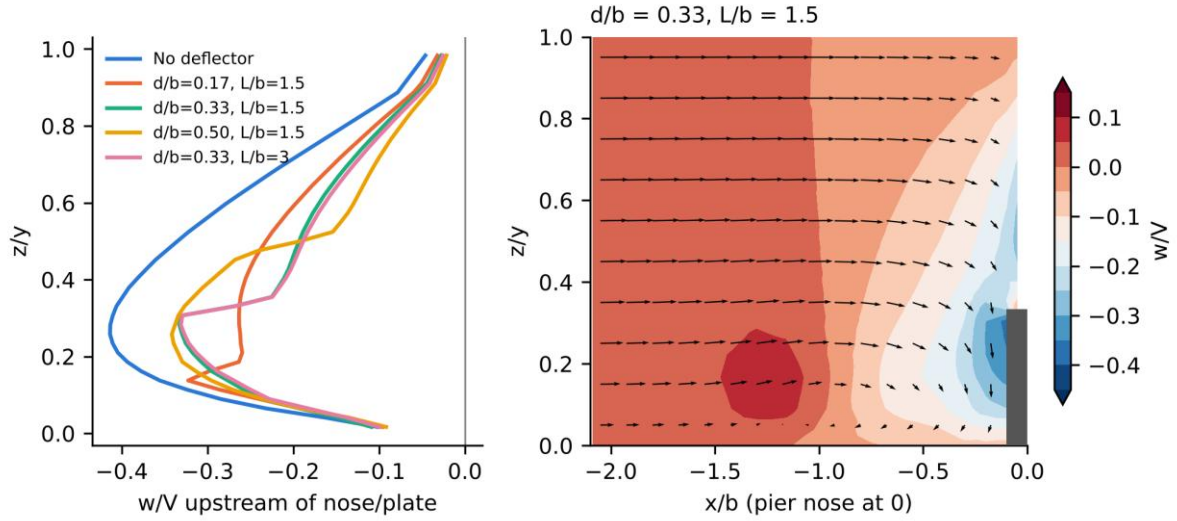


Fig. 12. Effect of the deflector on the downflow: (left) profiles just upstream of the nose/plate; (right) centre plane for d/b = 0.33, L/b = 1.5.

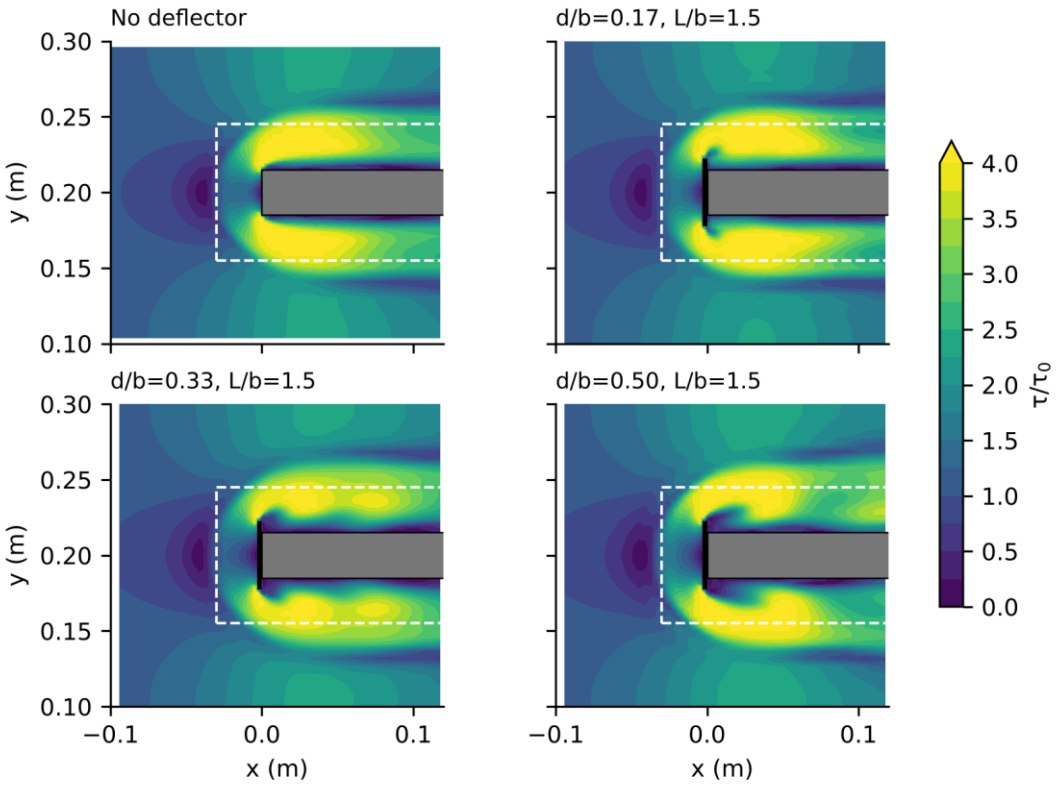


Fig. 13. Bed shear amplification around the pier nose for different deflector heights (L = 1.5b); dashed line: 3b collar.

3.8 Limitations

The model uses a rigid lid, which neglects free-surface deformation; this is acceptable for Fr ≤ 0.53 but less accurate at the highest Fr. Most cases use a flat, fixed bed and describe conditions at the start of scour. The scoured-bed cases use idealized holes of fixed shape; the collar was simulated in fixed holes, but the evolution of the hole and the deflector inside a hole were not simulated. The validation (Section 2.2.7) is for a single cylinder, and no velocity measurements were available for the present pier–abutment experiments. Steady RANS does not resolve the unsteady vortex shedding in the wakes. The laboratory runs lasted 6 h, so the measured depths may be slightly below the final equilibrium values, although the near-critical bed shear computed at the bottom of the measured holes (Sections 3.5–3.6) indicates that they were close to equilibrium. Peak shear at the sharp corners is not mesh-independent (Section 2.2.5). Simulating the evolving bed with a morphodynamic model (e.g. SSIIM, Sediment Simulation

In Intakes with Multiblock option, or SedFoam; Chauchat et al. 2017) and using detached-eddy simulation are recommended for further work.

4. Conclusions

(1) Validation against published velocity and bed-shear measurements in a scour hole (Graf and Istiarto 2002) showed that the model reproduces the peak downflow ($-0.59U$ versus $-0.60U$), its elevation, its radial decay and the onset of reversed bed shear.

(2) The approach-flow shear and the bed shear beyond about one pier width from the structures are mesh-independent (GCI < 5 %); the peak at the sharp corners is not and should be treated qualitatively. A continuous (Spalding) wall function is needed because the near-wall y^+ at the shear peaks lies at the switching point of the standard wall function.

(3) Bed shear is amplified about five times at the upstream corners of the pier and abutments, and the downflow at the pier nose reaches 0.41–0.43V on a flat bed. Inside an equilibrium scour hole it doubles to about 0.82V and sustains a horseshoe vortex with reverse near-bed velocity of about 0.66V.

(4) Bed-level collars shield the high-shear zones once their width exceeds about 2.5b; at $B_c/b \geq 4$ the peak amplification on the exposed bed falls to about 2.5–2.8 and changes little for wider collars, consistent with the diminishing return measured in the laboratory.

(5) A collar inside the scour hole intercepts the downflow at bed level, halving the downflow at the hole bottom and lowering the bottom shear from $0.93\tau_c$ to $0.41\tau_c$; with the collar's own measured hole the bottom shear is near critical ($0.73\tau_c$).

(6) With τ_c from the Shields criterion for the experimental sand, the computed excess shear explains the measured relative scour depth ($r = 0.95$; $r = 0.93$–0.95 using only mesh-

independent quantities), and the shear at the bottom of the equilibrium hole is close to critical.

(7) A vertical plate deflector at the pier nose reduces the peak downflow by about 20 %. A plate of height 0.33*b* and width 1.5*b* gives the most favorable shear ahead of the nose, matching the experimental optimum, while a wider plate (3*b*) creates high shear at its edges.

References

Baykal C, Sumer BM, Fuhrman DR, Jacobsen NG, Fredsøe J. Numerical investigation of flow and scour around a vertical circular cylinder. Philos Trans R Soc A. 2015; 373:20140104. https://doi.org/10.1098/rsta.2014.0104

Celik IB, Ghia U, Roache PJ, Freitas CJ, Coleman H, Raad PE. Procedure for estimation and reporting of uncertainty due to discretization in CFD applications. J Fluids Eng. 2008; 130:078001. https://doi.org/10.1115/1.2960953

Chauchat J, Cheng Z, Nagel T, Bonamy C, Hsu TJ. SedFoam-2.0: a 3-D two-phase flow numerical model for sediment transport. Geosci Model Dev. 2017; 10:4367–4392. https://doi.org/10.5194/gmd-10-4367-2017

Dey S. Three-dimensional vortex flow field around a circular cylinder in a quasi-equilibrium scour hole. Sadhana. 1995; 20:871–885.

Ebrahimi T, Hamidi M, Firoozjaee AR, Khavasi E. Collar effect on the pier scour: Eulerian–Lagrangian approach. Innov Infrastruct Solut. 2024; 9:448.

Ettema R, Constantinescu G, Melville BW. Flow-field complexity and design estimation of pier-scour depth: sixty years since Laursen and Toch. J Hydraul Eng. 2017; 143:03117006. https://doi.org/10.1061/(ASCE)HY.1943-7900.0001330

Graf WH, Istiarto I. Flow pattern in the scour hole around a cylinder. J Hydraul Res. 2002; 40:13–20. https://doi.org/10.1080/00221680209499869

393 Gupta LK, Pandey M, Anand Raj P, Pu JH. Scour reduction around bridge pier using the airfoil-
394 shaped collar. Hydrology. 2023; 10:77. https://doi.org/10.3390/hydrology10040077
395 Gupta LK, Pandey M, Anand Raj P. Numerical simulation of local scour around the pier with and
396 without airfoil collar (AFC) using FLOW-3D. Environ Fluid Mech. 2024; 24:631–649.
397 https://doi.org/10.1007/s10652-023-09932-2
398 Istiarto I. Flow around a cylinder in a scoured channel bed. Doctoral thesis No. 2368. Lausanne: École
399 Polytechnique Fédérale de Lausanne; 2001.
400 Khosronejad A, Kang S, Sotiropoulos F. Experimental and computational investigation of local scour
401 around bridge piers. Adv Water Resour. 2012; 37:73–85.
402 https://doi.org/10.1016/j.advwatres.2011.09.013
403 Kirkil G, Constantinescu G, Ettema R. Coherent structures in the flow field around a circular cylinder
404 with scour hole. J Hydraul Eng. 2008; 134:572–587. https://doi.org/10.1061/(ASCE)0733-
405 9429(2008)134:5(572)
406 Koken M, Constantinescu G. An investigation of the flow and scouring mechanisms around isolated
407 spur dikes in a shallow open channel: 1. Conditions corresponding to the initiation of the
408 erosion and deposition process. Water Resour Res. 2008; 44:W08406.
409 Melville BW. Pier and abutment scour: integrated approach. J Hydraul Eng. 1997; 123:125–136.
410 https://doi.org/10.1061/(ASCE)0733-9429(1997)123:2(125)
411 Melville BW, Coleman SE. Bridge scour. Highlands Ranch, CO: Water Resources Publications; 2000.
412 Menter FR. Two-equation eddy-viscosity turbulence models for engineering applications. AIAA J.
413 1994; 32:1598–1605. https://doi.org/10.2514/3.12149
414 Olsen NRB, Melaaen MC. Three-dimensional calculation of scour around cylinders. J Hydraul Eng.
415 1993; 119:1048–1054. https://doi.org/10.1061/(ASCE)0733-9429(1993)119:9(1048)
416 Pasha GA, Murtaza N, Hamidifar H. Collar systems for bridge pier scour protection. Innov Infrastruct
417 Solut. 2025; 10:557.

418 Raudkivi AJ. Functional trends of scour at bridge piers. J Hydraul Eng. 1986; 112:1–13.
419 https://doi.org/10.1061/(ASCE)0733-9429(1986)112:1(1)

420 Roulund A, Sumer BM, Fredsøe J, Michelsen J. Numerical and experimental investigation of flow and
421 scour around a circular pile. J Fluid Mech. 2005; 534:351–401.
422 https://doi.org/10.1017/S0022112005004507

423 Salaheldin TM, Imran J, Chaudhry MH. Numerical modeling of three-dimensional flow field around
424 circular piers. J Hydraul Eng. 2004; 130:91–100. https://doi.org/10.1061/(ASCE)0733-
425 9429(2004)130:2(91)

426 Soulsby RL. Dynamics of marine sands. London: Thomas Telford; 1997.

427 Spalding DB. A single formula for the law of the wall. J Appl Mech. 1961; 28:455–458.
428 https://doi.org/10.1115/1.3641728

429 Tafarojnoruz A, Gaudio R, Calomino F. Evaluation of flow-altering countermeasures against bridge
430 pier scour. J Hydraul Eng. 2012; 138:297–305. https://doi.org/10.1061/(ASCE)HY.1943-
431 7900.0000512

432 Tafarojnoruz A, Gaudio R, Dey S. Flow-altering countermeasures against scour at bridge piers: a
433 review. J Hydraul Res. 2010; 48:441–452. https://doi.org/10.1080/00221686.2010.491645

434 Wang C, Yu X, Liang F. A review of bridge scour: mechanism, estimation, monitoring and
435 countermeasures. Nat Hazards. 2017; 87:1881–1906. https://doi.org/10.1007/s11069-017-
436 2842-2

437 Weller HG, Tabor G, Jasak H, Fureby C. A tensorial approach to computational continuum mechanics
438 using object-oriented techniques. Comput Phys. 1998; 12:620–631.
439 https://doi.org/10.1063/1.168744

Supplementary Files

This is a list of supplementary files associated with this preprint. Click to download.

- AwaadWaterScienceSupplementaryrev1.docx